

A comparison of H-mode pedestal characteristics in MAST as a function of magnetic configuration and ELM type

A. Kirk, T. O’Gorman, S. Saarelma, R. Scannell, H.R. Wilson^a and the MAST team

EURATOM/UKAEA Fusion Association, Culham Science Centre, Abingdon, Oxon OX14 3DB, UK

^a*University of York, Heslington, York YO10 5DD UK*

Abstract

The H-mode pedestal characteristics on MAST are measured in a variety of Connected Double Null (CDN) and Single Null Divertor (SND) discharges. In CDN discharges the edge density pedestal width in spatial co-ordinates is similar on both the high and low field sides suggesting that the width may be determined by neutral penetration. However, in SND discharges the density pedestal width appears to be a flux surface quantity, which suggests that the scrape off layer may have a role to play in determining the density pedestal width. In both CDN and SND discharges the temperature pedestal width appears to be a flux surface quantity. The pedestal characteristics and edge stability have been studied as a function of ELM type. The edge temperature pedestal is found to have a weak dependence on ρ_{pol}^* , but increases with β_{pol} as $\Delta_{Te} \propto \beta_{pol}^{0.5}$.

1. Introduction

The reference scenario for ITER [1] is the high confinement mode (or H-mode) [2]. The improved confinement is the result of a transport barrier that forms at the plasma edge. Due to its influence on plasma performance, the pedestal formed by this barrier remains a critical area of fusion research and in order to develop a predictive capability it is necessary to understand what determines the pedestal characteristics in current devices.

The H-mode pedestal characteristics on MAST are measured using two Thomson scattering systems: a high spatial resolution single pulse Ruby system [3] and a 200 Hz Nd YAG system [4]. The Ruby system allows High (HFS) and Low (LFS) field side H-mode electron density and temperature profiles to be measured simultaneously, whereas the Nd YAG system has dedicated optics looking at the LFS plasma edge.

A previous study [5] of Connected Double Null (CDN) discharges in MAST using the Ruby system has shown that, even far in time from an ELM, the edge density pedestal width is not a flux surface quantity. Instead the HFS and LFS pedestal widths are similar in radial space. Although the temperature pedestal width could be measured at the HFS, temperatures below 100 eV could not then be measured reliably at the LFS due to limitations of the system, and hence no conclusion could be drawn about the temperature pedestal width variation between the HFS and LFS.

The pedestal widths were compared with an analytic model describing neutral penetration effects [5]. Although this model could describe the dependence of the density pedestal width with height it could not describe the characteristics of the HFS temperature pedestal and hence it is unlikely that neutral penetration alone determines the overall transport barrier width.

In this paper, new results on MAST H-mode pedestal characteristics from the new edge Nd YAG Thomson scattering system will be presented. In section 2 a comparison of the Ruby and Nd YAG systems will be made. In section 3 a comparison of the density and temperature pedestal widths at the HFS and LFS of CDN discharges will be presented and these will be compared with the widths observed in Single Null Divertor (SND) discharges. In section 4 a comparison of the pedestal properties as a function of ELM type will be discussed and in section 5 the scaling of the temperature pedestal width will be discussed.

2. Data selection and comparison of the Ruby and Nd YAG Thomson scattering systems

Plasmas in the Mega Ampere Spherical Tokamak (MAST) typically have a major radius, $R \sim 0.75$ m and a minor radius, $a \sim 0.5$ m. The data presented in this paper come from more than 300 analysed ELMy H-mode discharges when the plasma is either near to a Connected Double Null (CDN) or in a Lower Single Null Divertor (SND) configuration with the ion ∇B drift direction towards the lower targets. The discharges have a range of parameters with plasma current ~ 0.5 - 1.2 MA, Greenwald density ~ 0.2 - 0.9 , elongation ~ 1.6 - 2.1 , triangularity ~ 0.3 - 0.52 and $q_{95} \sim 3$ - 7 and a range of neutral beam heating powers 1.0 - 3.8 MW. The toroidal field on axis is in the range $0.45 \text{ T} < B_{\phi} < 0.55 \text{ T}$ and due to the low aspect ratio, the toroidal field varies between 1.7 T at the inboard mid-plane to 0.25 T at the outboard. This strong variation across the plasma is a distinct feature of the spherical tokamak.

The results presented in this paper come from either the MAST high-resolution Ruby Thomson scattering system [3], or the edge Nd YAG system [4]. The Ruby system measures, once per shot, the electron temperature (T_e) and density (n_e) profiles at 300 spatial points along a horizontal chord through the mid-plane of the plasma, which allows a simultaneous determination of both the HFS and LFS edge pedestals. The edge Nd YAG system consists

of 16 spatial points each separated by 1 cm and measures the density and temperature profiles at the LFS edge using 4 lasers each of which produces a profile every 20 ms [4]. The 4 lasers are aligned radially at the mid-plane and can measure temperatures down to 5 eV and densities down to $1 \times 10^{18} \text{m}^{-3}$. The lasers follow a slightly different path meaning that the radial position of each point is slightly different from one laser to another. By combining two of the Nd YAG lasers, which are fired within 1 μs of each other, it is possible to improve the spatial sampling to ~ 5 mm. In order to account for the difference in spatial resolution of the two TS systems the edge profiles have been fitted using a modified hyperbolic tangent (mtanh) function [6] convoluted with the instrument function representing the spatial resolution of the diagnostic. Figure 1a and b show the location of the laser paths superimposed on the poloidal cross section of a typical MAST a) CDN and b) lower SND equilibrium. The Ruby laser is located 15 mm below the centre of the machine and the Nd YAG laser 15 mm above. The two TS systems could not be synchronised for these experiments therefore a comparison of the system has been performed on discharges where the two systems were fired within 500 μs of each other and no large event (i.e. an ELM) occurred between the two laser times.

Figure 2 shows a comparison of the LFS density and temperature profiles obtained from the Ruby and Nd YAG systems in an inter-ELM period of a typical CDN H-mode discharge where both lasers fired within 20 μs of each other. Inside the pedestal region the profiles are in good agreement. The fact that the density pedestal profile in the steep region from the Ruby system is slightly broader than that from the Nd YAG system is due to the difference in spatial resolution between the Ruby (10 mm) and the Nd YAG (4 mm). In order to calculate the underlying widths (i.e. free from any smearing from the spatial resolution) the profiles are fitted with a mtanh function [6] convoluted with the instrument function for each system. The improved measurements of the temperature pedestal width using the Nd YAG

system can be observed from the temperature profile. The error bars from the Ruby system become large for values below ~ 120 eV whereas the Nd YAG system can measure well into the Scrape Off Layer (SOL).

The density profiles from the two systems have been fitted with a mtanh fit [6] taking into account the different spatial resolutions for all discharges where the lasers fired within 500 μ s of each other (43 discharges). A comparison of the pedestal density height (n_e^{ped}) and the density pedestal width (Δ_{n_e}) are shown in Figure 3 and demonstrate the good agreement between the two measurements.

3. Comparison of the HFS and LFS pedestal characteristics

The fact that the pedestal characteristics of the two systems are similar at the LFS, combined with the fact that only the Nd YAG system can resolve the LFS temperature pedestal, means that a comparison of the pedestal characteristics as a function of poloidal angle can be performed using the LFS from the Nd YAG system and the HFS data from the Ruby system. Such a comparison of the profiles for a single shot is shown in Figure 4 where the profiles are shown in normalised flux space. Note the LFS Nd YAG system (4 mm) has a similar spatial resolution to the HFS Ruby system (3 mm). Similar to what was reported previously [5] the density pedestal width is not the same in the normalised flux co-ordinate, being narrower at the HFS. However, the new data reveal that the electron temperature pedestal widths appear to be similar.

The density and temperature profiles from the two systems at the LFS and HFS in both radial and normalised flux space have been fitted with a mtanh fit taking into account the different spatial resolutions for all discharges where the lasers fired within 500 μ s of each other and no ELM or sawtooth crash occurred between the times of the two profiles (38 discharges). The density and temperature pedestal heights at the HFS and LFS determined

from these fits are similar. Figure 5 shows a comparison of the density (Δ_{n_e}) and temperature (Δ_{T_e}) pedestal width at the HFS and LFS in radial and flux space. As was observed previously the density pedestal width is not a flux surface quantity but is similar in radial space. However, the electron temperature pedestal width is a flux surface quantity. Since the lasers are located at approximately the same height the comparison in radial space requires no mapping, the comparison in flux space does depend on the equilibrium construction. As can be seen from Figure 1 there is approximately a factor of two difference in the flux expansion at the HFS compared to the LFS. This ratio is affected by the plasma pressure, which affects the Shafranov shift. The relative uncertainty in this ratio has been determined by a study of the uncertainties in the equilibrium and has been found to be less than 10 %. Hence uncertainties in the equilibrium can not explain the fact that the density pedestal is not a flux surface quantity.

The fact that there is a difference in the density and electron temperature widths can be highlighted further by calculating the ratio of the widths. Figure 6 shows the ratio of the temperature pedestal width to the density pedestal width, which have been measured in radial space to avoid any equilibrium mapping, for all CDN discharges where the profiles are obtained in inter-ELM periods (i.e. there is no requirement that the lasers fired at approximately the same time). The mean of the distribution at the HFS is approximately twice that at the LFS. This implies that across the pedestal region the electron pressure is not a flux surface quantity at each point and therefore that the total pressure must be balanced on each flux surface by either an asymmetry in the ion pressure or the dynamic pressure.

The most common operating mode for MAST is in a nearly CDN configuration in which the two X-points lie on approximately the same flux surfaces with the gap between these at the outboard mid-plane, δr_{sep} , being of the order of half the ion gyro-radius. As

δr_{sep} increases beyond this the power required to access H-mode increases strongly and hence there are no measurements of the pedestal characteristics in this region. However, H-mode can again be re-established, with a similar power to that required for CDN discharges, at much larger values of δr_{sep} in a lower SND configuration with the ion ∇B drift direction towards the lower X-point. In the CDN discharges the laser beams are located at approximately the height (z) of the magnetic axis of the plasma, however, in the SND discharges they are ~ 30 cm below (see Figure 1b). In order to allow a comparison with the pedestal widths in the CDN discharges, the profiles in the SND discharges are mapped to the z location of the magnetic axis. This mapping reduces the width measured at the height of the laser by ~ 0.85 in the SND discharges. The quoted widths in both cases are those at the z location of the magnetic axis.

The density pedestal width determined from the HFS and LFS density profiles from the Ruby Thomson scattering system for both the CDN and SND discharges are shown in Figure 7a in normalized flux space and in Figure 7b in radial space. The CDN discharges show the same behaviour as was observed in Figure 5 namely: the density pedestal width is not a flux surface quantity. In contrast, the density pedestal widths in the SND discharges are compatible with being flux surface quantities. For a given density pedestal height the density pedestal width at the LFS is effectively the same for the CDN and SND discharges. However, as is shown in Figure 7c, at the HFS the density pedestal width for a given density pedestal is larger in the SND discharges compared to the CDN discharges. It is difficult to see how neutral effects alone could explain this difference. A possible explanation for this is that the Scrape Off Layer (SOL) is playing a role in determining the pedestal width i.e. in the SND discharges processes occur in the SOL, which is connected between the LFS and HFS that act to broaden the HFS width.

Since there are fewer SND shots there are not sufficient examples where the Ruby and Nd YAG TS systems overlap in time to allow a comparison of the HFS and LFS profiles from the two systems. However, what can be compared is the ratio of the temperature pedestal width to the density pedestal width. Figure 8 shows this for all SND discharges at the LFS (using the Nd YAG system) and at the HFS (using the Ruby system). The ratio at the LFS is similar to that observed in the CDN shots (see Figure 6) but the ratio at the HFS is smaller than in the CDN case, which now results in the ratio being the same at the HFS and LFS. Since the density pedestal width is a flux surface quantity so is the temperature pedestal width.

In summary the only difference between the SND and CDN discharges is in the density pedestal width at the HFS. Although there is no clear explanation why the density pedestal width at the HFS is larger in the SND discharges, this data can be used to test models of pedestal formation.

4. *H-mode pedestal characteristics as a function of ELM type*

Figure 9 shows a plot of the electron temperature pedestal versus the density pedestal for both SND and CDN shots. First looking at the CDN discharges, these have been produced over a wide range of pedestal values. The standard mode of operation uses fuelling from a HFS mid-plane gas valve, as this has been found to reduce the power required for H-mode access [7]. The disadvantage of this technique is that due to the gas valve location, the gas flow cannot be turned off during the shot and hence there is very little control over the neutral density and hence plasma density. This results in the majority of discharges having pedestal densities of $3-5 \times 10^{19} \text{ m}^{-3}$ and temperatures of 50-150 eV with type III ELMs. Based on a study of ELM frequency with input beam power at a fixed plasma current and stability calculations, Type I ELMs typically occur for pedestal temperatures above 150 eV. In

addition, the minimum in the ELM frequency also occurs for pedestal temperatures of 150 eV as shown in Figure 10. Figure 10a shows the lowest ELM frequency observed in a given discharge with a plasma current of 750 kA as a function of power into the SOL (P_{SOL}), which is defined as the sum of the Ohmic and auxiliary power input to the core plasma less the rate of change of core stored energy and radiated power. A minimum in ELM frequency, which is usually associated with a transition from type III to type I ELMs, occurs at $P_{\text{SOL}} \sim 2.5$ MW. Figure 10b shows a plot of the average pedestal temperature in the H-mode period observed as a function of P_{SOL} . The temperature pedestal is typically above 150 eV for $P_{\text{SOL}} > 2.5$ MW corresponding to the transition to type I ELMs.

There is an additional set of discharges at low density ($n_e^{\text{ped}} < 2 \times 10^{19} \text{ m}^{-3}$) and high temperature ($T_e^{\text{ped}} > 150 \text{ eV}$) that have high frequency ELMs. These were previously christened type IV ELMs on DIII-D [8] though later renamed as the low collisionality branch of type III ELMs. Although this renaming seems appropriate, in order to investigate any differences between the low and high collisionality branch the type IV label has been retained in this paper. On MAST they are produced in discharges with greater than 3 MW of beam power and an optimised fuelling scenario using HFS upper and lower controlled gas valves. The SND shots typically have a smaller volume and surface area and hence a larger input power per unit volume and power per unit area across the LCFS. The pedestal electron pressure is higher than typically found in the CDN discharges and they are dominated by type I ELMs.

Figure 11 shows a plot of the electron temperature pedestal height versus the density pedestal height where the profiles were obtained in the last 10 % of the ELM cycle. The plot has been split up into ELM type: type I ELMs in CDN discharges (solid black circles), type III ELMs in CDN discharges (open blue diamonds), type IV ELMs in CDN discharges (open green triangles) and type I ELMs in SND discharges (open red squares). The SND discharges

clearly indicate a maximum pressure contour. The CDN discharges with type I ELMs are in the same region of space and in fact have a slightly higher pressure boundary. No indication of a pressure boundary is observed for the type III or type IV ELMs.

The edge stability is often described in terms of a current density versus normalised pressure gradient diagram [9]. In order to compare the MAST data with this picture the bootstrap current density profile has been calculated for each discharge from the measured density and temperature profiles at the LFS using the Sauter formula [10] and added to the Ohmic current profile obtained from the equilibrium (re-normalised so as to keep the total plasma current constant). The maximum parallel edge current density ($j_{//}$) is then determined from the peak in the current density profile. The normalised pressure gradient (α_{MHD}) has been calculated using the formula given in [11], which is the expression used in the ELITE stability code [12]. Figure 12a shows a plot of $j_{//}$ versus α_{MHD} as a function of ELM type for all the profiles obtained in the last 10 % of the ELM cycle. The type I ELMs from both the CDN and SND discharges are in a similar region of the diagram namely the top right hand corner, which is typically associated with the peeling ballooning boundary [9]. The type III ELMs occupy the lower left hand corner. In spite of the fact that the type IV ELMs are clearly separated from the type III ELMs in a plot of temperature versus density (Figure 11) they merge smoothly with the type III ELMs in the $j_{//}$ versus α_{MHD} diagram with the type IV ELMs having only a slightly higher edge current density for a given value of α_{MHD} compared to the type III ELMs. Since a possible picture in terms of known plasma instabilities is that type III ELMs are due to resistive ballooning modes whereas the type IV ELMs, which are obtained at lower collisionality, are peeling unstable driven by the edge current, a larger difference in $j_{//}$ may have been expected.

As shown in Figure 12b, a larger separation between type III and IV ELMs is seen in a plot of α_{MHD} versus pedestal collisionality (v_{ped}^*). There is a clear trend of decreasing α_{MHD}

with increasing v_{ped}^* in going from the type I to the type III ELMs. However, the type IV ELMs occupy a different region of the plot being at both low v_{ped}^* and low α_{MHD} .

Stability analyses have been performed, using the ideal MHD ELITE code [12], on 4 of the profiles obtained at the LFS just before an ELM in shots with different ELM types. The shots used are indicated in Figure 12a. Shot a is a CDN discharge with a type I ELM, shot b a CDN discharge with a type III ELM, shot c a CDN discharge with a type IV ELM and shot d a SND discharge with a type I ELM. The procedure used to analyse the edge stability in MAST has been described in [13]. It consists of reconstructing the equilibrium using the kinetic profiles obtained from the LFS Thomson Scattering (TS) system as constraints and assuming that $T_i = T_e$. As was discussed in section 3 the electron pressure in the CDN discharges is not a flux surface quantity at each point across the pedestal, therefore a choice has to be made between the HFS and LFS quantities. In this analysis the LFS profiles have been used since it has been assumed that the LFS determines the stability to ballooning modes. These profiles were fitted using a modified hyperbolic tangent taking into account the radial resolution of the TS system. The current profile is calculated by combining the bootstrap current, calculated using the formula given by Sauter [10], and the ohmic current. The edge pressure gradient is then varied at a fixed current density and the edge stability evaluated using ELITE [12]. Figure 13 shows the stability diagram obtained for the four discharges highlighted in Figure 12a representing typical a) type I ELMs in CDN, b) type III ELMs in CDN, c) type IV ELMs in CDN and d) type I ELMs in SND. In discharges a) and d) the experimental point lies close to the pressure and current boundary a trait often associated with type I ELMs. Both the type III and type IV discharges lie in a completely ideal MHD stable region. This suggests that these ELMs are associated with a resistive MHD stability, for example, resistive ballooning modes. If the current density is much higher than that estimated by the Sauter formula, then it is possible that peeling modes may play a role.

5. Dependence of the temperature pedestal width on plasma parameters

As was discussed earlier the density pedestal width can be influenced by neutrals and scrape off layer effects and so the temperature pedestal width is often used to represent the true transport barrier width. On MAST the temperature pedestal width as a function of temperature pedestal height is shown in Figure 14 as a function of ELM type. Each point represents the weighted mean of the data in that interval and the error bar represents the standard deviation of the distribution. For the type III and type I ELMs in both CDN and SND discharges there is an effectively linear rise of pedestal width with pedestal height. The type IV ELMs display a different dependence: after a linear rise the temperature pedestal width effectively saturates at a value of $\sim 11\text{mm}$. This may indicate that there is a different stability limit associated with this type of ELM or that there are other variables determining the width.

Several empirical scalings for the pedestal width (Δ_{ped}) have been proposed based on non-dimensional parameters such as the normalised poloidal ion Larmor radius (ρ_{pol}^*) or pressure (β_{pol}). However, there is a strong co-linearity between ρ_{pol}^* and β_{pol} in the pedestal region. In fact, DIII-D has shown that the widths scale as either $\Delta_{ped} = (\rho_{pol}^*)^{0.66}$ or as $\Delta_{ped} = (\beta_{pol})^{0.4}$ [14]. Recently, experiments on JT-60U have broken the co-linearity between ρ_{pol}^* and β_{pol} by comparing the pedestal widths in hydrogen and deuterium plasmas [15]. These measurements show that the width depends weakly on ρ_{pol}^* and more strongly on β_{pol} and a scaling of the form $\Delta_{ped} \propto (\rho_{pol}^*)^{0.2} (\beta_{pol})^{0.5}$ has been obtained.

Figure 15 shows a plot of β_{pol} versus ρ_{pol}^* as a function of ELM type for MAST data. As can be seen there is a strong correlation between the two variables for a given ELM type. However, the co-linearity can be broken by looking at either a different magnetic

configuration or different ELM type. i.e. by comparing type I ELMs in SND and CDN discharges, a region can be found where the β_{pol} is the same but the ρ_{pol}^* is different. By comparing different ELM types, discharges can be found that have the same ρ_{pol}^* but different β_{pol} . For example discharges have been chosen where the β_{pol} is between 0.24 and 0.35. This selects out two sets of data consisting of type I ELMs in CDN and SND discharges. For each set the mean values of ρ_{pol}^* and normalized temperature pedestal width (Δ_{T_e}/a) are calculated. Figure 16a shows these mean values (open red circles) together with error bars representing the standard deviation of the distribution. There is no evidence for a rise of width with ρ_{pol}^* . The same technique has been used in the β_{pol} range between 0.12 and 0.15 (solid black circles) and again there is no evidence for any co-linearity. Conversely Figure 16b shows what happens if data is selected to have a constant ρ_{pol}^* range and a plot is made of the mean normalised temperature width against β_{pol} . In this case a clear increase of Δ_{T_e}/a with β_{pol} is observed. This is consistent with the results obtained from JT-60U that show that the rise in temperature pedestal width is due to the increase in β_{pol} and not ρ_{pol}^* .

Figure 17a shows a plot of normalized temperature pedestal width versus β_{pol} for the entire data set as a function of ELM type. Each point represents the weighted mean of the data in that interval and the error bar represents the standard deviation of the distribution. In all cases the normalized width increases with β_{pol} but the increase is less than linear. A fit to each distribution to the form $\Delta_{T_e}/a = A_{T_e} \times \beta_{\text{pol}}^{B_{T_e}}$. While the values of A_{T_e} differ between the CDN and SND data the values of B_{T_e} from all the fits are consistent with 0.5 i.e. $B_{T_e} = 0.52 \pm 0.03$ (CDN type I), 0.49 ± 0.03 (CDN type III) and 0.47 ± 0.05 (SND). A similar dependence of the temperature pedestal width with β_{pol} has been observed on ASDEX Upgrade [16].

On DIII-D and C-Mod a scaling of the pressure pedestal with $\sqrt{\beta_{pol}}$ has been reported [16]. Figure 17b shows a plot of normalized pressure pedestal width versus β_{pol} on MAST as a function of ELM type, where it can be seen that the pedestal widths for type III ELMs have a different dependence to those for type I ELMs. A fit to each distribution to the form $\Delta_{P_e}/a = A_{P_e} \times \beta_{pol}^{B_{P_e}}$ gives $B_{P_e} = 0.56 \pm 0.04$ (CDN type I), 0.27 ± 0.05 (CDN type III) and 0.51 ± 0.03 (SND). The pressure pedestal dependence for type I ELMs is similar to that observed on DIII-D and C-Mod, but type III ELMs have a different dependence. For completeness, the normalised density pedestal width is plotted Figure 17c, similar to as was seen in the pressure pedestal width, the density pedestal width dependence for the type III ELMs is different to that observed for the type I ELMs. It can also be seen that the pressure pedestal width is smaller than both the density and temperature pedestal widths, which is due to the fact that the temperature and density barrier positions are at different locations.

On DIII-D the pressure pedestal width in normalised flux space has been showed to scale as $\Delta P_e = A_{P_e} \sqrt{\beta_{pol}}$, where $A_{P_e} = 0.07$ [16]. In order to allow a comparison of this parameter across devices the MAST profiles have also been fitted in normalised flux space. Again the pressure pedestal width is found to be consistent with increasing proportional to $\sqrt{\beta_{pol}}$. A fit to the form $\Delta P_e = A_{P_e} \sqrt{\beta_{pol}}$ gives $A_{P_e} = 0.07$ (CDN type I ELMs) and 0.056 (SND type I), parameters consistent with those observed on DIII-D. However, the DIII-D value of 0.07 comes from a fit to the average density and temperature width i.e. $(\Delta T_e + \Delta n_e)/2$. As can be seen from Figure 17, on MAST the density and temperature pedestal widths are greater than the measured pressure pedestal width so here a fit to $(\Delta T_e + \Delta n_e)/2 = A_{av} \sqrt{\beta_{pol}}$ yields $A_{av} = 0.13$ (CDN type I ELMs) and 0.19 (SND type I), which does not agree with the DIII-D value.

6. Summary and conclusions

The H-mode pedestal characteristics on MAST are measured in a variety of plasma conditions using two independent Thomson scattering systems. The High and Low Field Side H-mode density and temperature profiles are fitted taking into account the resolution due to the instrument function, which enables a study of the poloidal variation of pedestal quantities to be made. In CDN plasmas, the density pedestal width is not a flux surface quantity but rather is found to be similar in radial space at both the HFS and LFS, which suggests a role of neutrals in determining the density pedestal width. In contrast, the density pedestal width is a flux surface quantity in SND discharges, suggesting some interaction between the scrape off layer and the density pedestal width. In both the CDN and SND discharges the temperature pedestal width is a flux surface quantity.

The temperature pedestal characteristics have been studied as a function of ELM type. Stability calculations using the ELITE code show that profiles obtained just before type I ELMs lie close to the peeling-ballooning boundary but type III and type IV ELMs appear to be stable. The temperature pedestal width is found to increase weakly, if at all, with ρ_{pol}^* , but increases with β_{pol} as $\Delta_{Te} \propto \beta_{pol}^{0.5}$.

Acknowledgements

UKAEA authors were funded jointly by the United Kingdom Engineering and Physical Sciences Research Council and by the European Communities under the contract of

Association between EURATOM and UKAEA. The views and opinions expressed herein do not necessarily reflect those of the European Commission.

References

- [1] ITER Physics Expert Group, Nucl. Fusion **39** (1999) 2391.
- [2] F. Wagner *et al.*, Phys. Rev. Lett. **49** (1982) 1408.
- [3] M.J. Walsh *et al.*, Review of Scientific Instruments **74** (2003) 1663.
- [4] R. Scannell *et al.*, Review of Scientific Instruments **77** (2006) 10E510.
- [5] A. Kirk *et al.*, Plasma Phys. Control. Fusion **46** (2004) A187.
- [6] R.J. Groebner and T.N. Carlstrom, Plasma Phys. Control. Fusion **40** (1998) 673.
- [7] A.R. Field *et al.*, Plasma Phys. Control. Fusion **46** (2004) 981.
- [8] R. Maingi *et al.*, J. Nucl Mater. **337-339** (2005) 727.
- [9] H.R. Wilson *et al.*, Plasma Phys. Control. Fusion **48** (2006) A71.
- [10] O. Sauter, C. Angioni and Y.R. Lin-Liu, Physics of Plasmas **6** (1999) 2834.
- [11] R.L. Miller *et al.*, Physics of Plasmas **5** (1998) 973.
- [12] H.R. Wilson *et al.*, Physics of Plasmas **9** (2002) 1277.
- [13] S. Saarelma *et al.*, Plasma Phys. and Control. Fusion **49** (2007) 31.
- [14] T. Osborne *et al.*, Plasma Phys. Control. Fusion **40** (1998) 845.
- [15] H. Urano *et al.*, Nucl. Fus. **48** (2008) 045008.
- [16] P. Snyder *et al.*, 'Pedestal Stability Comparison and ITER Pedestal Prediction', IT/P6-14 presented at the 22nd IAEA Fusion energy conference, Geneva, Switzerland, 2008.

Figures

Figure 1 Poloidal cross section of a) a CDN and b) a lower SND equilibrium. The positions of the horizontal Ruby and Nd YAG Thomson scattering system are indicated by dashed and dotted lines respectively.

Figure 2 Comparison of the a) density and b) electron temperature profiles obtained from the Ruby and Nd YAG Thomson scattering systems at the low field side in a CDN discharge.

Figure 3 Comparison of a) density pedestal height and b) density pedestal width at the LFS from the Ruby and Nd YAG Thomson scattering systems in CDN discharges.

Figure 4 Comparison of the a) density and b) electron temperature profiles at the HFS from the Ruby TS system with the LFS from the Nd YAG TS system in a CDN discharge.

Figure 5 Comparison of a) the density pedestal width, b) electron temperature pedestal width in radial space and c) the density pedestal width, d) electron temperature pedestal width in normalised flux space at the HFS from the Ruby TS system and at the LFS from the Nd YAG TS system in CDN discharges.

Figure 6 Ratio of temperature and density pedestal widths in radial space at LFS (using Nd YAG TS system) and HFS (using Ruby TS system) in CDN discharges.

Figure 7 Comparison of a) the density pedestal width in normalised flux space, b) the density pedestal width in radial space and c) the density pedestal width versus density pedestal height at the HFS from the Ruby TS system for CDN (solid black circles) and SND (open red squares) discharges.

Figure 8 Ratio of temperature and density pedestal widths in radial space at the LFS (using Nd YAG TS system) and HFS (using Ruby TS system) in SND discharges.

Figure 9 Electron temperature pedestal height versus density pedestal height for all shots.

Figure 10 a) Minimum ELM frequency and b) temperature pedestal height versus P_{SOL} in CDN discharges.

Figure 11 Electron temperature pedestal height versus density pedestal height as a function of ELM type from profiles obtained in the last 10 % of the ELM cycle.

Figure 12 As a function of ELM type and for profiles obtained in the last 10 % of the ELM cycle: a) peak edge parallel current density (j_{\parallel}) versus normalised pressure gradient (α_{MHD}) and b) α_{MHD} versus pedestal collisionality (ν_{ped}^*).

Figure 13 Stability diagram plots from ELITE showing edge current density versus normalised pressure gradient for different examples of ELM type and magnetic configurations. (The circles represent unstable locations, squares stable locations and the diamond is the experimentally measured point). a) Type I ELM, b) type III ELM and c) type IV ELM in CDN discharges and d) a type I ELM in a SND discharge.

Figure 14 Temperature pedestal width (Δ_{Te}) versus temperature pedestal height (T_e^{ped}) as a function of ELM type.

Figure 15 Normalised poloidal pressure (β_{pol}) versus normalised poloidal larmor radius (ρ_{pol}^*) as a function of ELM type.

Figure 16 Normalised temperature pedestal width (Δ_{Te}/a) versus a) ρ_{pol}^* for fixed β_{pol} and b) β_{pol} for fixed ρ_{pol}^* .

Figure 17 a) Normalised temperature pedestal width (Δ_{Te}/a), b) normalised pressure pedestal width (Δ_{pe}/a) and c) normalised density pedestal width (Δ_{ne}/a) versus β_{pol} as a function of ELM type.

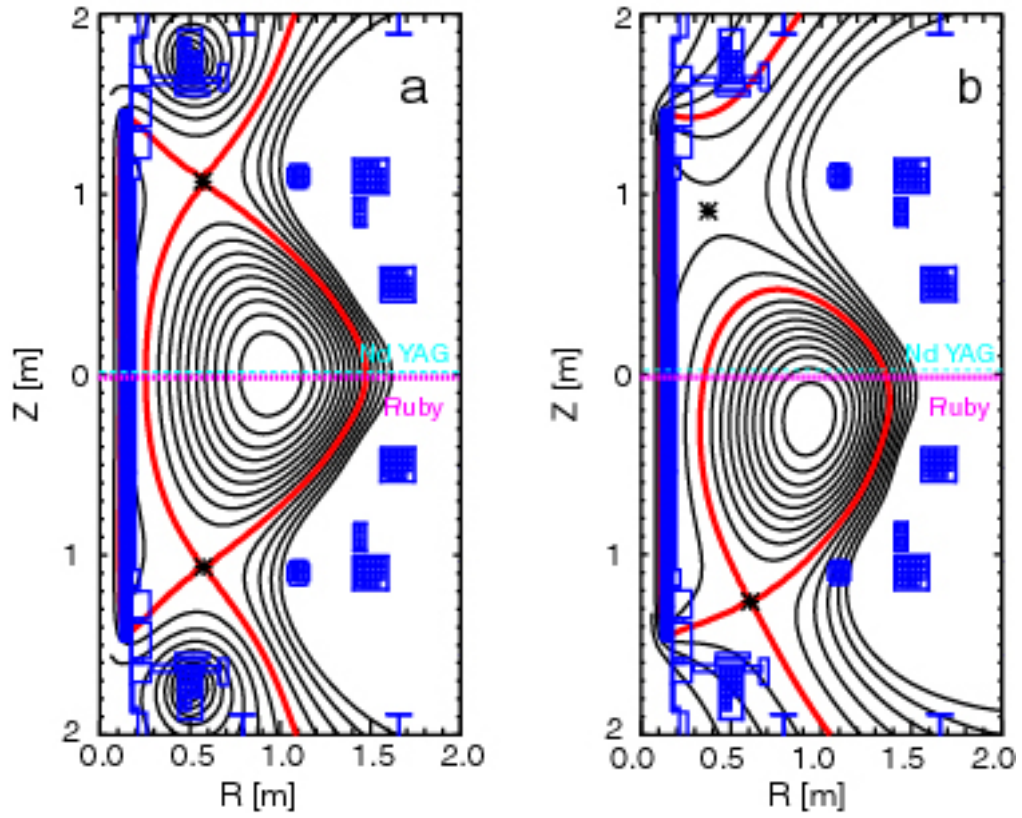


Figure 1 Poloidal cross section of a) a CDN and b) a lower SND equilibrium. The positions of the horizontal Ruby and Nd YAG Thomson scattering system are indicated by dashed and dotted lines respectively.

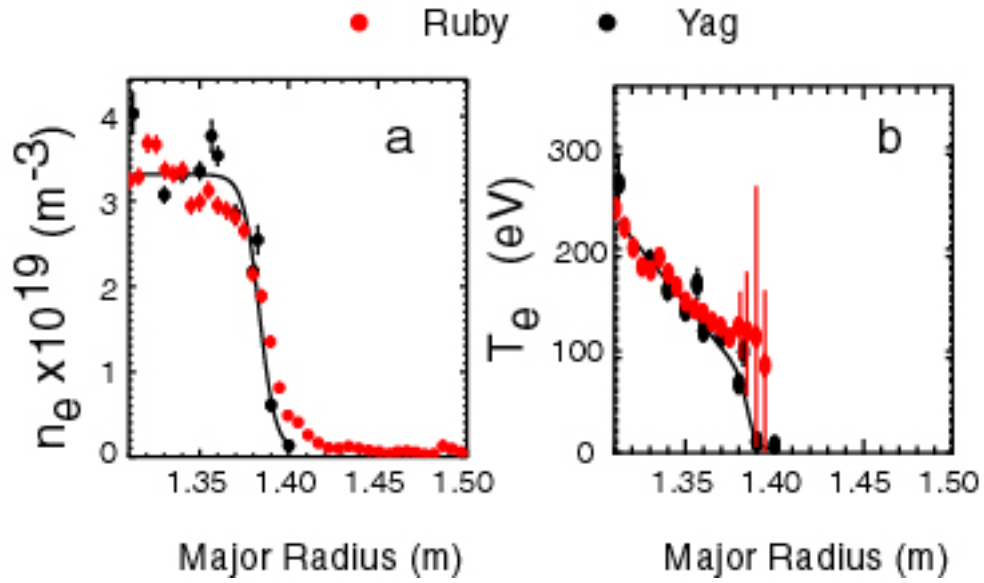


Figure 2 Comparison of the a) density and b) electron temperature profiles obtained from the Ruby and Nd YAG Thomson scattering systems at the low field side in a CDN discharge.

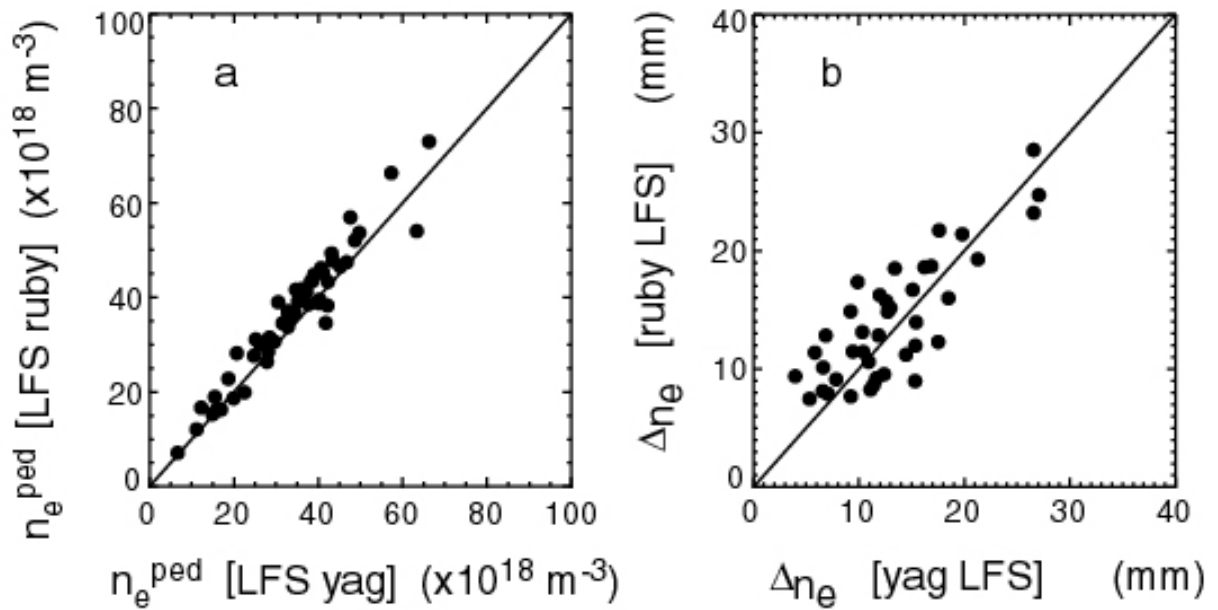


Figure 3 Comparison of a) density pedestal height and b) density pedestal width at the LFS from the Ruby and Nd YAG Thomson scattering systems in CDN discharges.

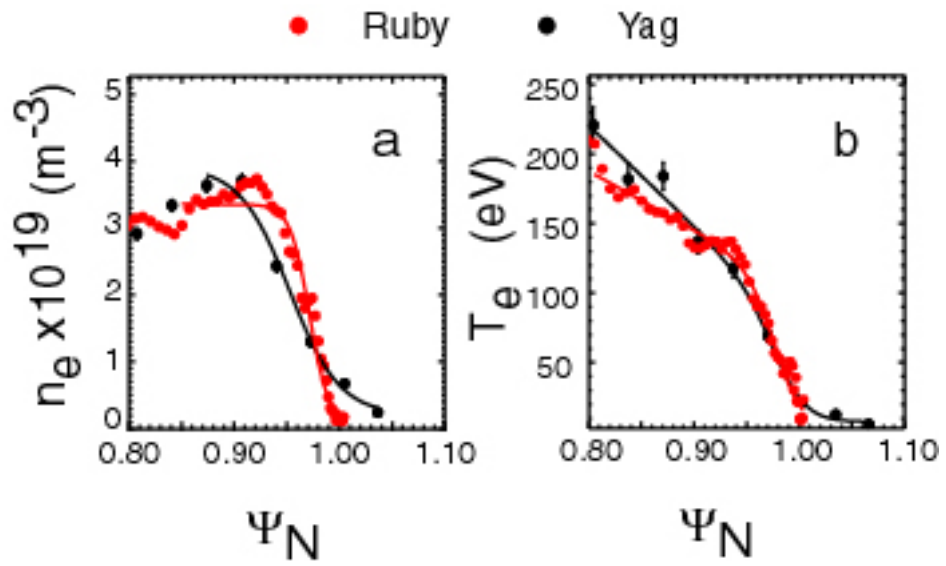


Figure 4 Comparison of the a) density and b) electron temperature profiles at the HFS from the Ruby TS system with the LFS from the Nd YAG TS system in a CDN discharge.

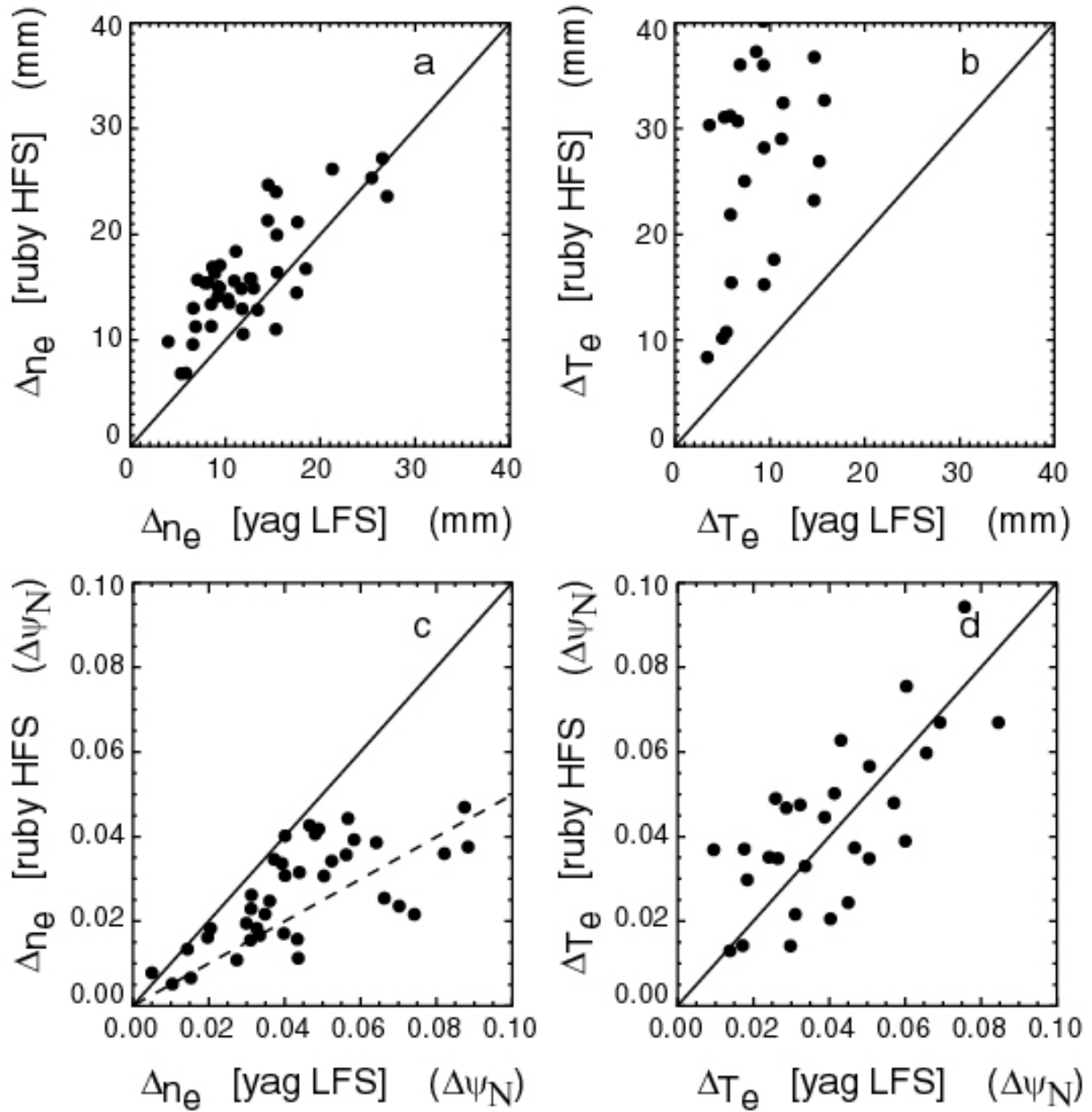


Figure 5 Comparison of a) the density pedestal width, b) electron temperature pedestal width in radial space and c) the density pedestal width, d) electron temperature pedestal width in normalised flux space at the HFS from the Ruby TS system and at the LFS from the Nd YAG TS system in CDN discharges.

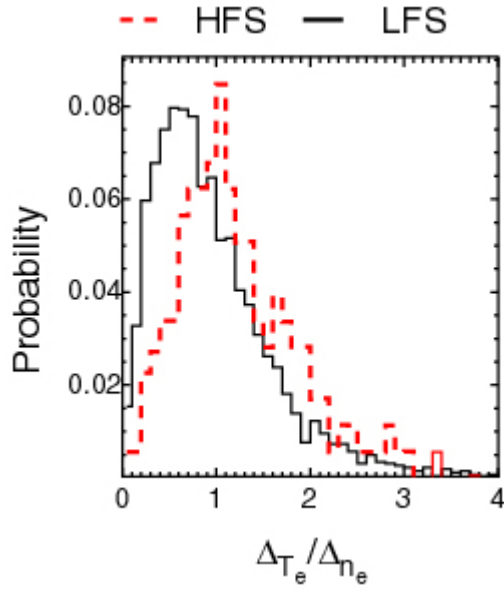


Figure 6 Ratio of temperature and density pedestal in radial space widths at LFS (using Nd YAG TS system) and HFS (using Ruby TS system) in CDN discharges.

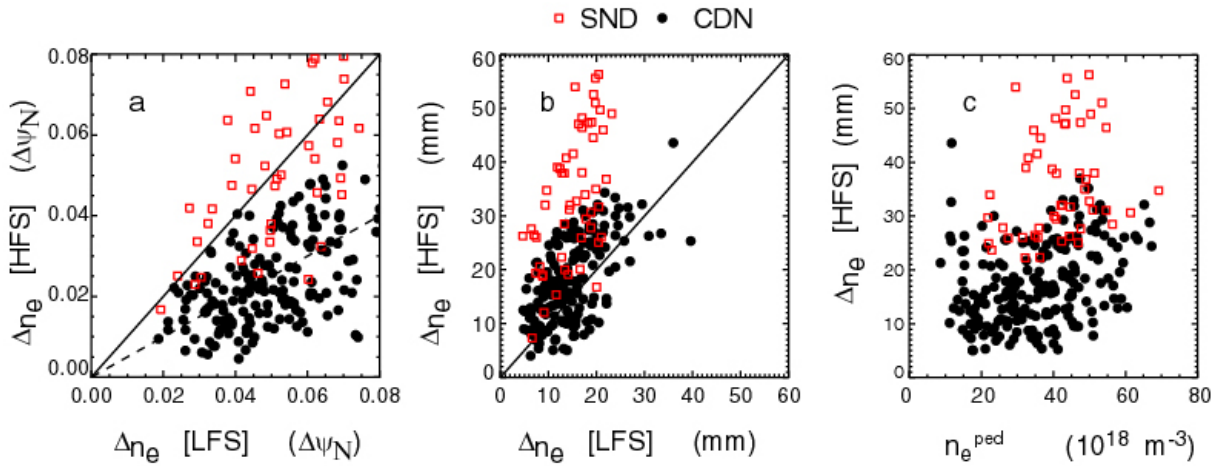


Figure 7 Comparison of a) the density pedestal width in normalised flux space, b) the density pedestal width in radial space and c) the density pedestal width versus density pedestal height at the HFS from the Ruby TS system for CDN (solid black circles) and SND (open red squares) discharges.

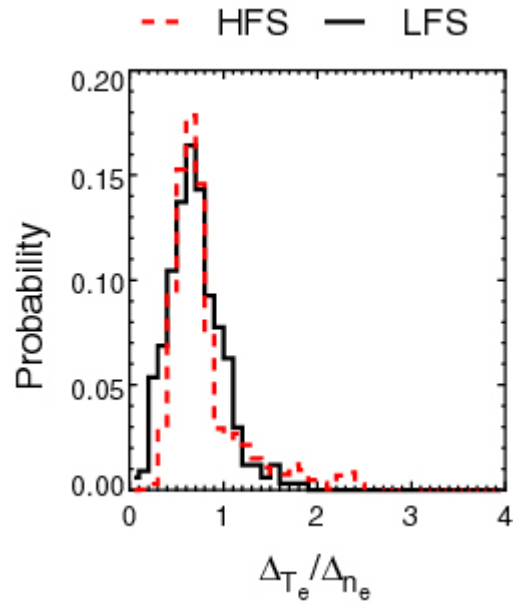


Figure 8 Ratio of temperature and density pedestal widths in radial space at the LFS (using Ng YAG TS system) and HFS (using Ruby TS system) in SND discharges.

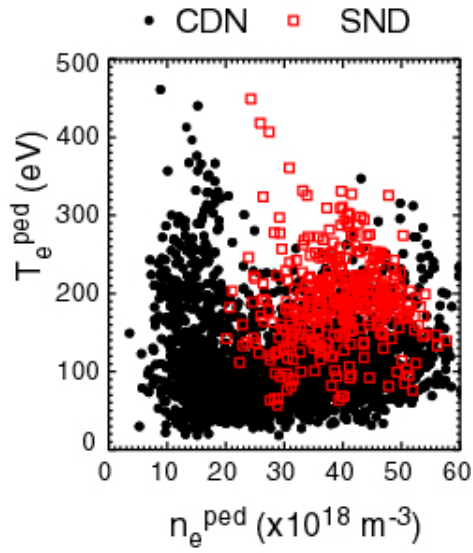


Figure 9 Electron temperature pedestal height versus density pedestal height for all shots.

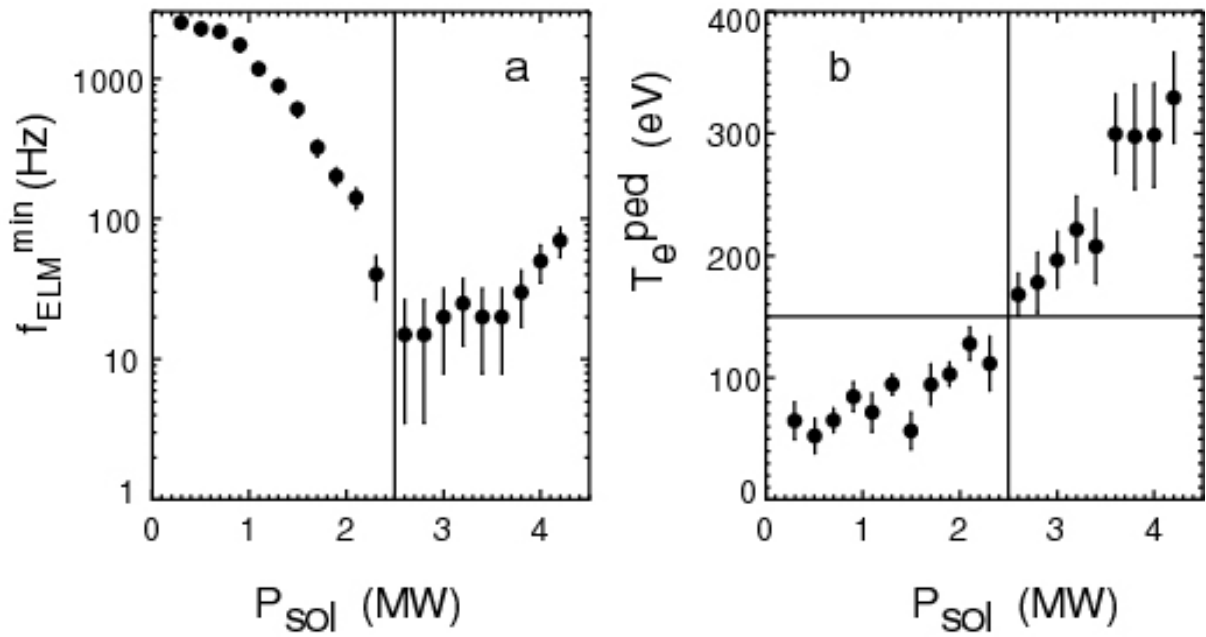


Figure 10 a) Minimum ELM frequency and b) temperature pedestal height versus P_{sol} in CDN discharges.

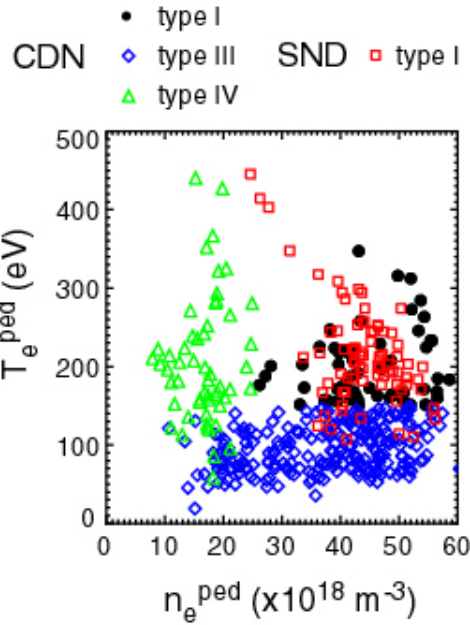


Figure 11 Electron temperature pedestal height versus density pedestal height as a function of ELM type from profiles obtained in the last 10 % of the ELM cycle.

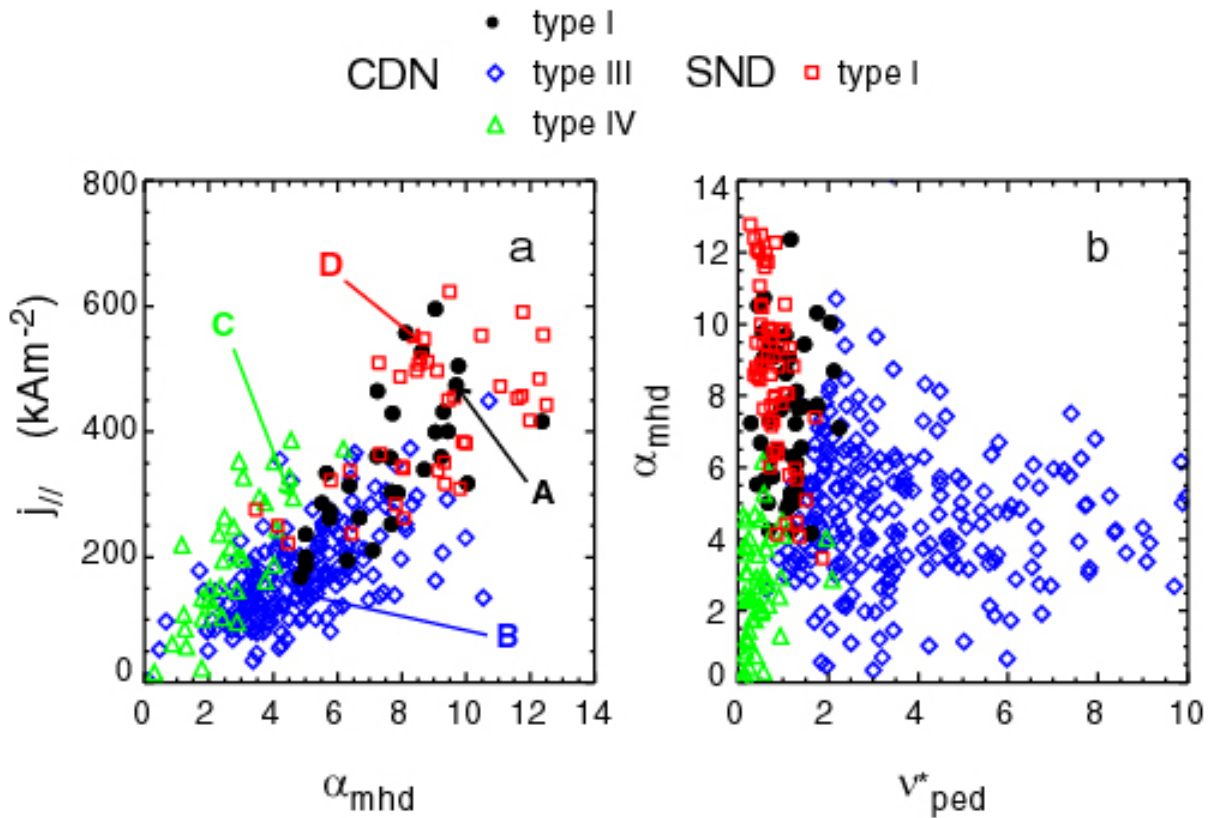


Figure 12 As a function of ELM type and for profiles obtained in the last 10 % of the ELM cycle: a) peak edge parallel current density ($j_{||}$) versus normalised pressure gradient (α_{MHD}) and b) α_{MHD} versus pedestal collisionality (v_{ped}^*).

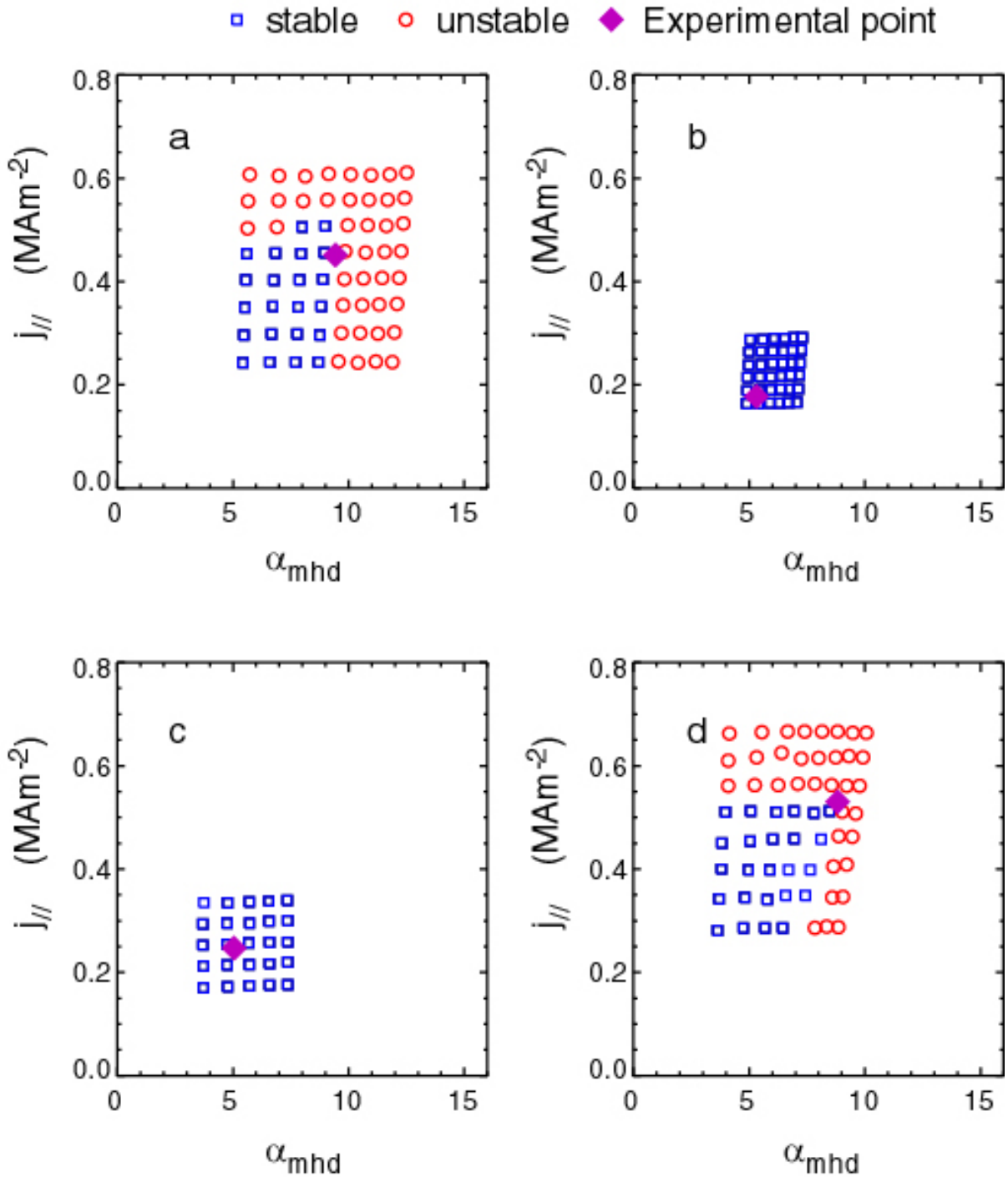


Figure 13 Stability diagram plots from ELITE showing edge current density versus normalised pressure gradient for different examples of ELM type and magnetic configurations (The circles represent unstable locations, squares stable locations and the diamond is the experimentally measured point). a) Type I ELM, b) type III ELM and c) type IV ELM in CDN discharges and d) a type I ELM in a SND discharge.

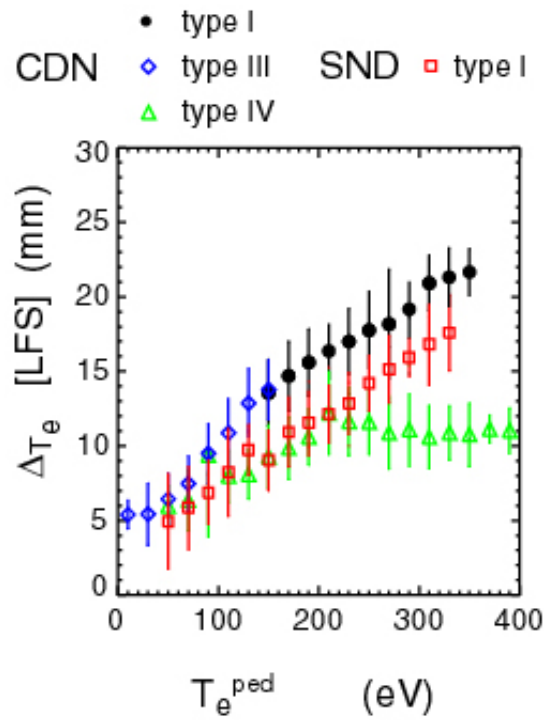


Figure 14 Temperature pedestal width (ΔT_e) versus temperature pedestal height (T_e^{ped}) as a function of ELM type.

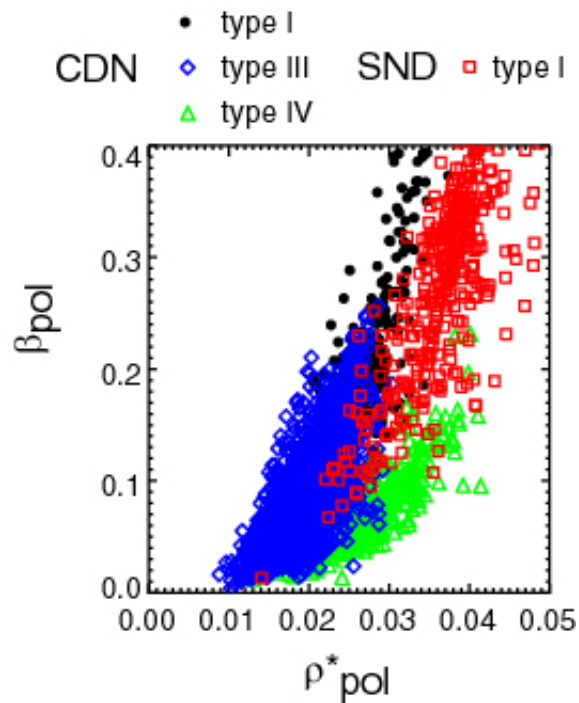


Figure 15 Normalised poloidal pressure (β_{pol}) versus normalised poloidal larmor radius (ρ_{pol}^*) as a function of ELM type.

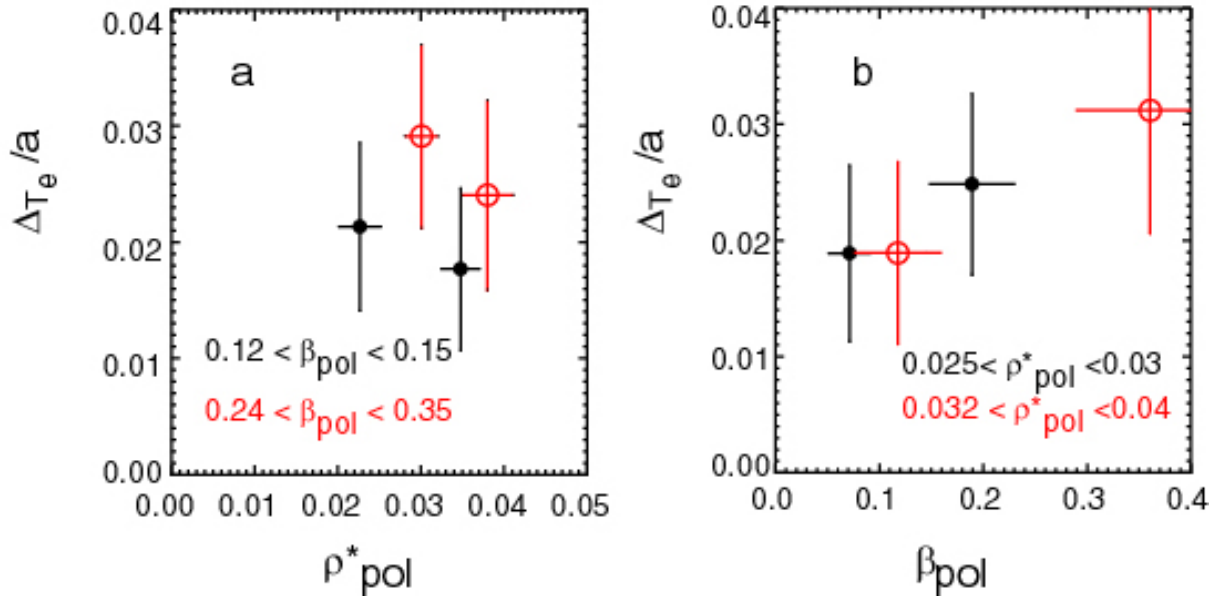


Figure 16 Normalised temperature pedestal width ($\Delta T_e/a$) versus a) ρ^*_{pol} for fixed β_{pol} and b) β_{pol} for fixed ρ^*_{pol} .

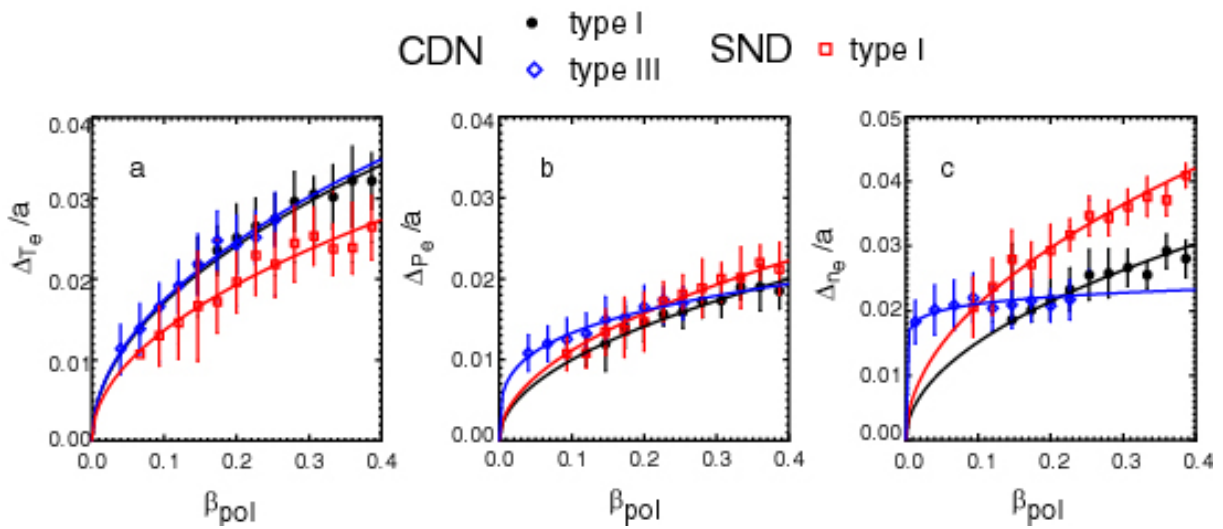


Figure 17 a) Normalised temperature pedestal width ($\Delta T_e/a$), b) normalised pressure pedestal width ($\Delta P_e/a$) and c) normalised density pedestal width ($\Delta n_e/a$) versus β_{pol} as a function of ELM type.